

Thermal behavior of borax, $\text{Na}_2\text{B}_4\text{O}_5(\text{OH})_4 \cdot 8\text{H}_2\text{O}$

WATARU NISHIYASU¹ AND ATSUSHI KYONO^{1,*}

¹Division of Earth Evolution Sciences, Graduate School of Life and Environmental Sciences, University of Tsukuba, 1-1-1 Tennodai, Tsukuba 305-8572, Japan

ABSTRACT

Globally, borax is one of the most important borate minerals, both industrially and from a technological viewpoint. Despite its importance, there have been only a few reports on the structural changes of borax upon heating. In this study, we have investigated the thermal behavior and structural characteristics of borax using thermal analysis, in situ high-temperature synchrotron X-ray diffraction, in situ variable-temperature single-crystal X-ray diffraction, and quantum chemical calculations. Differential scanning calorimetry (DSC) curve showed a large endothermic peak at 349 K corresponding to the dehydration reaction of borax. X-ray diffraction (XRD) pattern remained almost unchanged up to 353 K. Above 363 K, the XRD peaks gradually became less intense until they disappeared at 403 K. The unit-cell volume continuously increased with increasing temperature and became constant just before its phase transition to tinalconite. The volumetric thermal expansion coefficient between 113 and 323 K was $7.84 \times 10^{-5} \text{ K}^{-1}$. The *a* and *c* lattice parameters exhibited a slight increase trend with increasing temperature, whereas the *b* lattice parameter increased significantly. Therefore, the thermal expansibilities followed the order $b/b_0 \gg c/c_0 > a/a_0$. The increasing *b* lattice parameter was closely related to the elongation of the $\text{O4} \cdots \text{H7B}$ hydrogen-bond interaction along the *b*-axis. Na–O bond lengths were isotropically expanded with increasing temperature, whereas the B–O bond lengths and angles remained unchanged even after the phase transition to tinalconite. Molecular orbital calculations revealed that an electron cloud shared by two borate tetrahedra led to the formation of a large electron cloud distribution over the $\text{B}_4\text{O}_5(\text{OH})_4$ cluster. The intramolecular interactions with substantial covalent character made the cluster quite rigid. The existence of borate minerals containing the $\text{B}_4\text{O}_5(\text{OH})_4$ clusters in their structure evidenced the presence of moderately acidic or alkaline water, wherein the borate minerals grew via the incorporation of $\text{B}_4\text{O}_5(\text{OH})_4$ clusters. Our results indicate that the connection geometry of the fundamental building block consisting of $\text{B}\phi_3$ triangles and $\text{B}\phi_4$ tetrahedra (ϕ : O^{2-} , OH^-) can potentially be used as a palaeoenvironmental indicator.

Keywords: Borax, sodium tetraborate decahydrate, dehydration, single-crystal X-ray diffraction, powder X-ray diffraction, quantum chemical calculation

INTRODUCTION

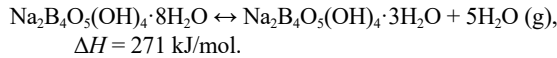
The cosmic scarcity of boron has resulted in a low boron concentration in the solar system. The boron concentration can be approximated from type CI carbonaceous chondrite, coming out at 0.78 ppm (Shearer and Simon 2017). Earth's primitive mantle was accordingly depleted in boron. The boron concentration in fresh MORB is lower than 1 ppm (Wunder et al. 2005); however, its extrusion is accompanied by the release of boron into seawater. Thus, boron is gradually concentrated in seawater, resulting in a boron concentration of 4.5 ppm (Wunder et al. 2005). Subsequently, the sediment pore water and hydrous minerals, including the seawater are carried to the continental crust, which is presently a typical reservoir of boron. The current estimated average boron concentration reaches 17 ppm (Rudnick and Gao 2014). Since boron is incompatible with many silicate minerals (Bindeman et al. 1998), it is further concentrated into residual melts during rock formation. Consequently, the boron concentration in

granitic pegmatites, which is the largest reservoir of boron, falls within the range of 213–287 ppm (Stilling et al. 2006; Simmons et al. 2016). Thereafter, weathering causes boron to dissolve into the surface water, which flows out and is gathered in basins to form large non-marine evaporite boron deposits (Helvacı and Palmer 2017). Currently major commercial resources of borates are colemanite $\text{CaB}_3\text{O}_4(\text{OH})_3 \cdot \text{H}_2\text{O}$, ulexite $\text{NaCaB}_3\text{O}_6(\text{OH})_6 \cdot 5\text{H}_2\text{O}$, borax $\text{Na}_2\text{B}_4\text{O}_5(\text{OH})_4 \cdot 8\text{H}_2\text{O}$, tinalconite $\text{Na}_2\text{B}_4\text{O}_5(\text{OH})_4 \cdot 3\text{H}_2\text{O}$, and kernite $\text{Na}_2\text{B}_4\text{O}_6(\text{OH})_2 \cdot 3\text{H}_2\text{O}$. These are dominant in Turkey, the United States, and Russia, which together supply more than 80% of the world's borate (Helvacı and Palmer 2017).

Borax is one of the most important borate minerals worldwide. From an industrial and technological point of view, borax is a valuable research material owing to its broad applications, including borosilicate glasses, glass wool, ceramics, cement enamels, and detergents (Garrett 1998). Borax is closely related to its dehydration product tinalconite, $\text{Na}_2\text{B}_4\text{O}_5(\text{OH})_4 \cdot 3\text{H}_2\text{O}$. Indeed, the two minerals interconvert rapidly and reversibly at a relative humidity of 60% and temperatures of 20–25 °C (Christ and Garrels 1959). In addition, the dehydration–hydration reaction between borax

* E-mail: kyono@geol.tsukuba.ac.jp. Orcid 0000-0001-5419-390X

and tinalconite can store and release a large amount of latent heat as follows:



Notably, this value is almost six times larger than the latent heat of the phase transition between liquid water and vapor (Rossini et al. 1952). Therefore, borax is also an important phase change material (PCM) that is attracting significant attention owing to its high energy storage capacity (Raoux and Wuttig 2009; Sharma et al. 2009; Zhou et al. 2012).

Despite its great importance, to date, there are few reports on the crystal structure changes of borax during the heating process (Waclawska 1995; Ekmekyapar et al. 1997; Dumanli et al. 2022; Nishiyasu and Kyono 2023). Therefore, in this study, we investigated the thermal behaviors and structural features of borax using thermal analysis, in situ high-temperature synchrotron X-ray diffraction, in situ variable-temperature single-crystal X-ray diffraction, and quantum chemical calculation.

EXPERIMENTAL METHODS

Commercially available borax, sodium tetraborate decahydrate (guaranteed reagent grade, Fujifilm Wako Pure Chemical, Osaka, Japan), was used as the starting

material. First, single crystals of borax were recrystallized from a saturated aqueous solution of borax at 293 K. Thermal analysis was performed by differential scanning calorimetry (DSC) using a thermal analyzer (X-DSC7000, Seiko Instruments, Chiba, Japan). Approximately 10 mg each of borax and α -alumina reference were placed into flat-bottomed aluminum pans. Each sample was first cooled to 143 K at a cooling rate of 10 K/min and subsequently heated across the temperature range from 143 to 323 K with a heating rate of 10 K/min. Measurement was performed under argon gas flow at a rate of 50 mL/min.

In situ high-temperature synchrotron powder XRD measurements were performed at BL-8B of the Photon Factory (PF), High Energy Accelerator Research Organization (KEK), Japan. The incident beam was monochromatized using a Si(111) double-crystal monochromator. The X-ray wavelength was determined to be 0.6841(1) Å using CeO_2 (NIST Standard Reference Material 674a), while the X-ray beam was collimated to a diameter of 0.5 mm. Data were recorded on a large Debye-Scherrer camera with a radius of 191.3 mm equipped with a curved imaging plate (IP) detector (R-AXIS RAPID, Rigaku Corporation, Tokyo, Japan). The borax powder was inserted into a Lindemann glass capillary ($\phi = 0.7$ mm) with one end fully opened. The capillary was then mounted and aligned with a goniometer, introduced into a heating furnace, and subsequently heated under an ambient atmosphere at a fixed temperature step of 10 K from 303 to 473 K. After reaching a target temperature, the sample was maintained at this temperature for 5 min before the data were collected. The actual temperature was estimated in advance by direct measurement at the sample position using a chromel–alumel type K thermocouple. The oscillation method was used with an oscillation angle $\Delta\omega = 10^\circ$ and the X-ray exposure time was 3 min for one measurement. IP data was integrated into a two-dimensional pattern using the Rigaku software (Rapid-Auto, Rigaku Corporation, Tokyo, Japan).

A single crystal, approximately $0.1 \times 0.1 \times 0.05$ mm in size, was selected under a stereoscopic microscope (SMZ1270, Nikon Corporation, Tokyo, Japan) and fixed

TABLE 1. Crystal data and summary of the parameters of data collection and structural refinement for borax

Temperature (K)	113	143	173	203	233
	Crystal data				
Crystal system	monoclinic	monoclinic	monoclinic	monoclinic	monoclinic
Space group	<i>C2/c</i>	<i>C2/c</i>	<i>C2/c</i>	<i>C2/c</i>	<i>C2/c</i>
<i>a</i> (Å)	11.843(5)	11.853(5)	11.854(5)	11.851(5)	11.861(5)
<i>b</i> (Å)	10.535(5)	10.556(5)	10.569(5)	10.582(5)	10.605(4)
<i>c</i> (Å)	12.165(5)	12.175(5)	12.177(5)	12.176(5)	12.182(5)
β (°)	106.870(5)	106.846(5)	106.772(5)	106.735(5)	106.724(5)
<i>V</i> (Å ³)	1452.5(11)	1458.0(11)	1460.7(11)	1462.2(11)	1467.4(11)
<i>Z</i>	4	4	4	4	4
	Data collection and refinement				
Maximum observed 2θ (°)	57.98	57.93	57.89	57.85	58.08
Measured reflections	4353	4374	4386	4418	4439
Unique reflections	1756	1769	1783	1783	1786
Reflections $F_o > 4\sigma(F_o)$, R_{int}	1586, 0.0322	1618, 0.0340	1621, 0.0257	1608, 0.0265	1574, 0.0298
Range of <i>h, k, l</i>	$-15 \leq h \leq 13$ $-13 \leq k \leq 14$ $-16 \leq l \leq 8$	$-15 \leq h \leq 13$ $-13 \leq k \leq 14$ $-16 \leq l \leq 8$	$-15 \leq h \leq 13$ $-13 \leq k \leq 14$ $-16 \leq l \leq 8$	$-15 \leq h \leq 13$ $-13 \leq k \leq 14$ $-16 \leq l \leq 8$	$-15 \leq h \leq 13$ $-13 \leq k \leq 14$ $-16 \leq l \leq 8$
<i>R1</i> [$F_o > 4\sigma(F_o)$]	0.0334	0.0317	0.0303	0.0294	0.0339
<i>wR2</i>	0.1010	0.0906	0.0884	0.0891	0.0967
Goodness of fit	1.098	1.041	1.066	1.065	1.053
Number of l.s. parameters	147	147	147	147	147
Residual highest and deepest peaks ($e/\text{Å}^3$)	0.30, -0.27	0.30, -0.30	0.34, -0.25	0.32, -0.23	0.31, -0.24
Temperature (K)	263	293	323		
	Crystal data				
<i>a</i> (Å)	11.868(5)	11.868(5)	11.863(6)		
<i>b</i> (Å)	10.624(4)	10.642(4)	10.653(5)		
<i>c</i> (Å)	12.195(5)	12.198(5)	12.187(6)		
β (°)	106.628(5)	106.579(5)	106.537(6)		
<i>V</i> (Å ³)	1473.2(10)	1476.6(10)	1476.4(12)		
<i>Z</i>	4	4	4		
	Data collection and refinement				
Maximum observed 2θ (°)	57.97	57.91	57.95		
Measured reflections	4454	4464	4446		
Unique reflections	1793	1799	1808		
Reflections $F_o > 4\sigma(F_o)$, R_{int}	1604, 0.0257	1588, 0.0284	1505, 0.0220		
Range of <i>h, k, l</i>	$-15 \leq h \leq 13$ $-13 \leq k \leq 14$ $-16 \leq l \leq 8$	$-15 \leq h \leq 13$ $-13 \leq k \leq 14$ $-16 \leq l \leq 8$	$-15 \leq h \leq 13$ $-13 \leq k \leq 14$ $-16 \leq l \leq 8$		
<i>R1</i> [$F_o > 4\sigma(F_o)$]	0.0315	0.0339	0.0336		
<i>wR2</i>	0.0899	0.0982	0.0945		
Goodness of fit	1.065	1.071	1.062		
Number of l.s. parameters	147	147	147		
Residual highest and deepest peaks ($e/\text{Å}^3$)	0.30, -0.21	0.30, -0.23	0.28, -0.24		

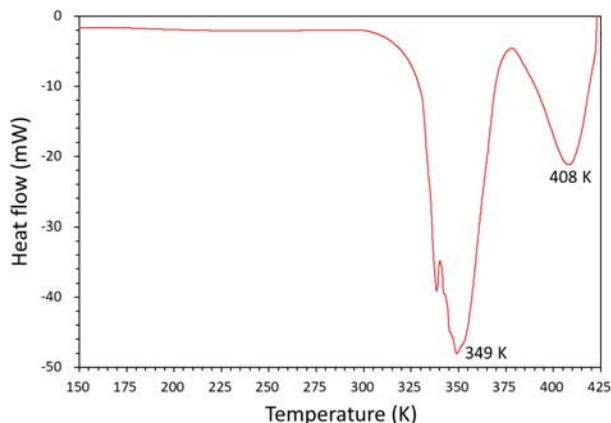


FIGURE 1. DSC curve of borax obtained using a heating rate of 10 K/min. (Color online.)

in a 0.7 mm Lindemann glass capillary with nitrocellulose adhesive dissolved in acetone to prevent dryness and degradation of the single crystal during measurement. Determination of the lattice parameters and intensity data collection were performed using a single-crystal diffractometer (Smart Apex II Ultra Bruker AXS, Karlsruhe, Germany) equipped with a CCD detector, multilayer optics, and graphite monochromated $\text{MoK}\alpha$ radiation ($\lambda = 0.71073 \text{ \AA}$) generated by a rotating anode. The in situ variable-temperature single-crystal X-ray diffraction measurements were performed using a N_2 -gas-flow cryostat (DX-CS190LD, Japan Thermal Engineering, Sagamihara, Japan) with a temperature accuracy of $\pm 1 \text{ K}$. The actual sample temperature was estimated in advance at the sample position with a chromel-alumel thermocouple. The single crystal in the capillary was mounted on the diffractometer and then cooled down to 113 K in the cryostat. The measurements were performed during the heating procedure from 113 to 323 K with a 30 K step. The heating experiment of borax was terminated at 323 K because of the loss of crystallinity at 333 K. The initial lattice parameters and orientation matrix were determined from 36 frames collected with an exposure time of 5 s. A total of 720 frames were collected with an exposure time per frame of 5 s using the ω -scan mode with $\Delta\omega = 0.5^\circ$ at three different ϕ positions. Intensity data were integrated and corrected for Lorentz polarization effects using APEX3 software (Bruker 2018). The collected data were reduced using the SAINT software package (Bruker 2017). Empirical absorption correction was also applied using SADABS software (Sheldrick 2012). The structure was solved by a combination of the direct method and the difference Fourier methods provided by the program package SHELXS-2013/1 (Sheldrick 2008). The atomic coordinates and atomic displacement parameters were refined by full-matrix least-squares methods on F^2 using the program SHELXL-2014/7 (Sheldrick 2008). The atomic labels were taken from the reported structure (Levy and Lisensky 1978). Hydrogen positions were refined using the constraint that the OH bond length is 0.95 Å, while for the H_2O molecules, the atomic distance between the H atoms was constrained to 1.50 Å. All atoms, except for the H atoms, were refined on the basis of the anisotropic displacement model. The data collection and crystal structure refinement (CIF¹) details are listed in Table 1.

Ab initio quantum chemical calculations of the electronic structure were performed with the density functional theory method (RB3LYP) with the 6-311+G basis set, using the quantum chemical calculation software package Gaussian-16 (Frisch et al. 2016). The structural model was built based on the atomic coordinates experimentally determined by the single-crystal X-ray diffraction measurement at 113 K. The cell dimension of the simulation region was approximately $-0.1 \leq x \leq 1.1$, $-0.7 \leq y \leq 0.7$, $0.5 \leq z \leq 1.1$, which includes one $\text{B}_4\text{O}_7(\text{OH})_4$ cluster constituting two BO_4 tetrahedra and two BO_3 triangles surrounded by 12 $\text{Na}(\text{H}_2\text{O})_6$ polyhedra. The molecular orbital (MO) surfaces were rendered with the GaussView molecular visualization package (Dennington et al. 2016), and the MOs were drawn at an interface value of 0.02 au.

RESULTS AND DISCUSSION

Phase transition from borax to tinalconite

Figure 1 shows the DSC curve of borax. The first large endothermic peak started at 331 K and reached a maximum at 349 K.

A previous study showed the first endothermic peak as being centered at 347 K (Waclawska 1995). This peak corresponds to the dehydration reaction of borax, which suggests that the phase transition from borax to tinalconite occurred. The second endothermic peak, which corresponds to the dehydration reaction of tinalconite, starts at 383 K and reaches a maximum at 408 K. We previously confirmed by TG-DTA measurement that after the dehydration of tinalconite, the TG curve shows a continuous mass loss up to approximately 1073 K (Nishiyasu and Kyono 2023).

Figure 2 illustrates the continuous variation in the XRD pattern of borax as a function of temperature. The XRD pattern observed at 303 K was in excellent agreement with that of borax. The peak intensities of borax remained almost unchanged until 353 K. Above 363 K, the borax peaks gradually became less intense until they were no longer observed at 403 K. In contrast, the peaks of tinalconite started to appear above 353 K. The tinalconite peaks remained at low intensity and continued to appear up to 473 K. The difference in the dehydration temperature between the XRD and DSC measurements was attributed to the measurement conditions of an open vs. a semi-open system.

Thermal structural changes in borax

The crystal structures of borate minerals contain clusters of corner-sharing $\text{B}\phi_3$ triangles and $\text{B}\phi_4$ tetrahedra (ϕ : O^{2-} , OH^-) that polymerize to form large clusters, chains, sheets, or frame-

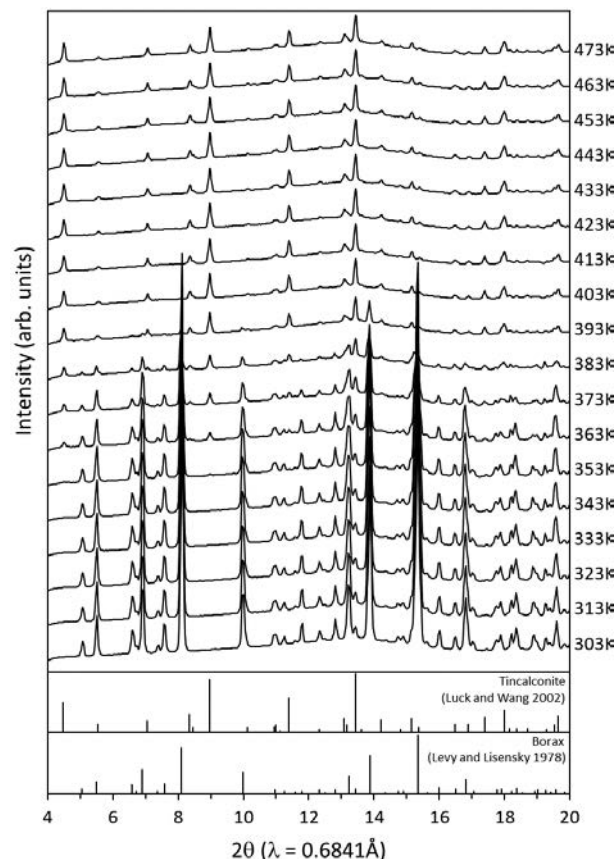


FIGURE 2. In situ high-temperature synchrotron powder X-ray diffraction patterns in the temperature range of 303–473 K.

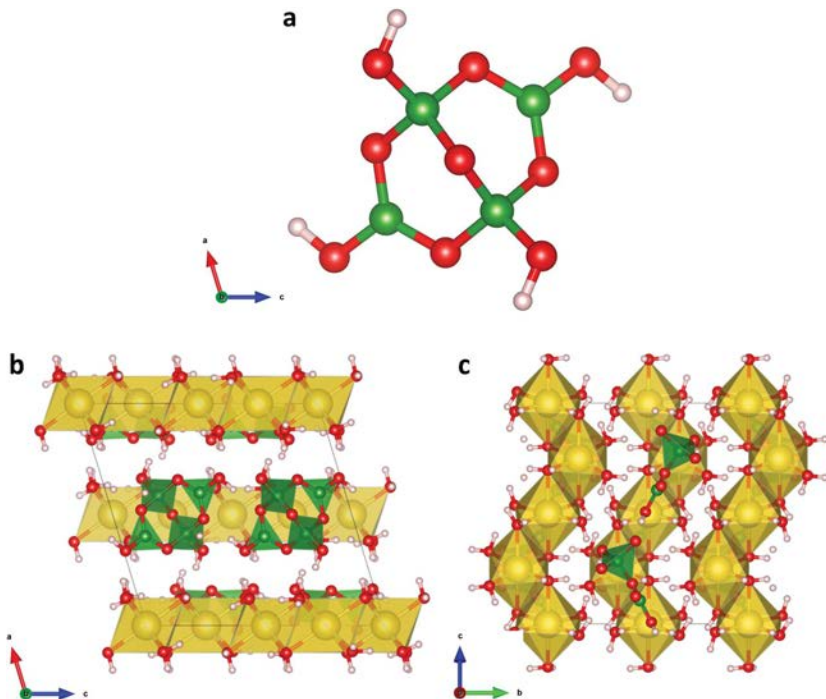


FIGURE 3. (a) Fundamental building block (FBB) of an isolated $\text{B}_4\text{O}_5(\text{OH})_4$ cluster consisting of two triangular and two tetrahedral coordination units linked by common O atoms to form a double ring. This FBB is expressed as $\langle\Delta 2\Box\rangle=\langle\Delta 2\Box\rangle$ (Burns et al. 1995). Crystal structure of borax viewed in the direction of the (b) b -axis and (c) a -axis. Sodium, boron, oxygen, and hydrogen atoms are shown as yellow, green, red, and pink spheres, respectively. Sodium atoms are coordinated by six O atoms, whereas boron atoms are coordinated by four or three O atoms. (Color online.)

works. The borate structures are, therefore, classified based on the connection geometry of this fundamental building block (FBB) consisting of borate polyhedra. Figure 3 shows the crystal structure of borax. The FBB in the borax crystal structure is an isolated $\text{B}_4\text{O}_5(\text{OH})_4$ cluster consisting of two $\text{BO}_2(\text{OH})$ triangles and two $\text{BO}_3(\text{OH})$ tetrahedra linked by common O atoms to form a double ring with two common tetrahedra (Fig. 3a). According to the structural representation proposed by Burns et al. (1995), the FBB is expressed as $2\Delta 2\Box:\langle\Delta 2\Box\rangle=\langle\Delta 2\Box\rangle$, where Δ and \Box represent the $\text{B}\phi_3$ triangle and $\text{B}\phi_4$ tetrahedron, respectively. The FBBs are linked by hydrogen bonding with adjacent zigzag chains of edge-sharing $\text{Na}(\text{H}_2\text{O})_6$ octahedra running along the c -axis. The zigzag chains are further stacked together along the a - and b -axes. Figure 4 displays the variations in the lattice parameters determined by the single-crystal X-ray measurements. The a and c lattice parameters exhibited a slight increase trend with increasing temperature, whereas the b lattice parameter significantly increased. Because $\sin \beta$ increases with the decrease in β from 106.870° to 106.537° (Table 1), the decrease in β results in an increase in the unit cell volume ($V=abc \sin \beta$). Consequently, the unit cell volume continuously increased with increasing temperature but became constant just before the phase transition to tincalconite. Because water oxygen or hydroxyl O atoms might be partially released from borax at 323 K, we tried to refine the site occupancy factors of the water oxygen and hydroxyl O atoms in borax. However, our results show that they remained at approximately ± 1.0 within the experimental error. Thus neither the water molecules nor the hydroxyl O atoms were yet lost from borax at this temperature. This indicates that borax loses its single crystallinity immediately after dehydration. The volumetric thermal expansion coefficient between 113 and 323 K is calculated by the equation:

$$\alpha_V = (1/V_0) \times [(V_1 - V_0)/(T_1 - T_0)]$$

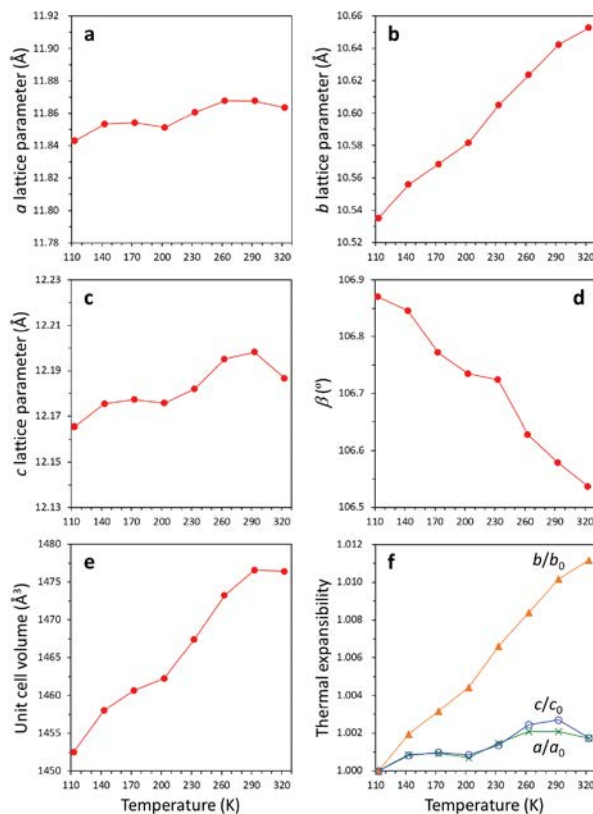


FIGURE 4. Variations in lattice parameters (a) a , (b) b , (c) c , (d) β , (e) unit-cell volume, and (f) expansibility of the lattice as a function of temperature. (Color online.)

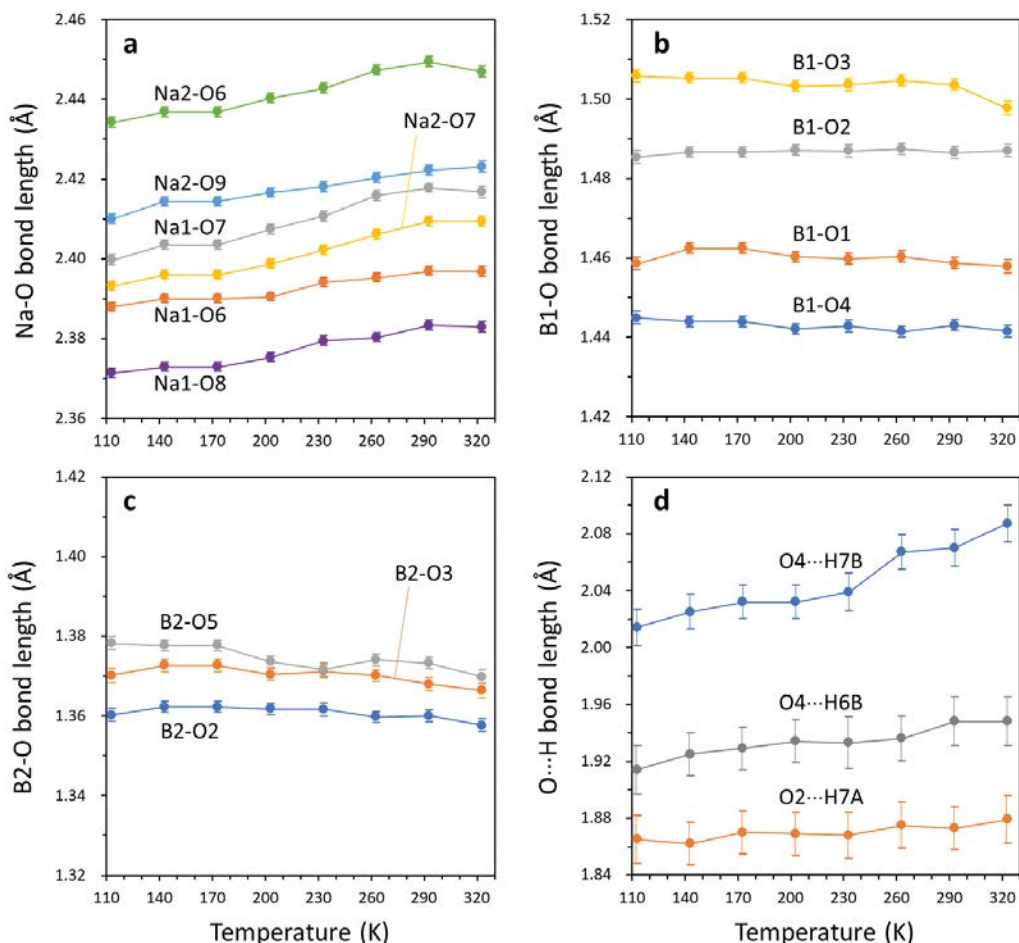


FIGURE 5. Variations in the (a) Na-O, (b) B1-O, (c) B2-O, and (d) O...H bond lengths as a function of temperature. (Color online.)

was $7.84 \times 10^{-5} \text{ K}^{-1}$. For lattice parameters a , b , and c , the thermal expansion coefficients obtained between 113 and 323 K were $\alpha_a = 8.04 \times 10^{-6} \text{ K}^{-1}$, $\alpha_b = 5.33 \times 10^{-5} \text{ K}^{-1}$, and $\alpha_c = 8.61 \times 10^{-6} \text{ K}^{-1}$, respectively. The thermal expansibilities therefore followed the order $b/b_0 \gg c/c_0 > a/a_0$ and the thermal expansion was most sensitive to temperature along the b -axis.

The fractional atomic coordinates and displacement parameters are listed in Online Materials¹ Table S1. The variations in the selected bond lengths are given in Online Materials¹ Table S2 and plotted in Figure 5. The Na-O bond lengths were isotropically expanded with temperature; however, the Na2-O6 and Na1-O7 bond lengths slightly decreased at 323 K. Consequently, since the Na2-O6 and Na1-O7 bonds lie in the ac plane, the a and c lattice parameters also slightly decreased at 323 K. The variation in the hydrogen bonds between the FBB and zigzag chain is shown in Figure 5d. The three selected hydrogen bonds, O2...H7A, O4...H7B, and O4...H6A are oriented toward the a -, b -, and c -axis, respectively. It is apparent that the increasing b lattice parameter is closely related to the elongation of the O4...H7B hydrogen bond interaction along the b -axis (Fig. 5d). The most characteristic point in this study is that the B-O bond lengths remained almost unchanged or even slightly decreased with increasing temperature (Figs. 5b and 5c). The crystal structure of lithium tetraborate

($\text{Li}_2\text{B}_4\text{O}_7$) possesses the same FBB connection geometry as that of borax (Krogh-Moe 1962), which is expressed as $\langle \Delta 2 \square \rangle = \langle \Delta 2 \square \rangle$ (Fig. 3a). Senyshyn et al. (2010) previously investigated the structural changes of $\text{Li}_2\text{B}_4\text{O}_7$ at low temperature from 3.4 to 268 K using neutron powder diffraction. They reported that the variations in the B-O bond lengths in the triangular and tetrahedral coordination were within 0.01 and 0.015 Å, respectively (Senyshyn et al. 2010). Sennova et al. (2007), on the other hand, investigated the structural changes of $\text{Li}_2\text{B}_4\text{O}_7$ at high temperatures, in the range from 293 to 773 K, using in situ high-temperature X-ray powder diffraction. Their results revealed that in this temperature range, the individual B-O bond length changes were insignificantly small (≤ 0.005 Å). The study by Sennova et al. (2007) suggested that the $\langle \Delta 2 \square \rangle = \langle \Delta 2 \square \rangle$ cluster was extremely stable as an FBB, even under high-temperature conditions. It can be, therefore, concluded that the B-O bond lengths in the borax FBB are essentially unaffected by temperature. In addition, tincalconite possesses the exact $\text{B}_4\text{O}_5(\text{OH})_4$ cluster as that of borax in its structure (Fig. 3a) (Giacovazzo et al. 1973; Luck and Wang 2002). These $\text{B}_4\text{O}_5(\text{OH})_4$ clusters in tincalconite are directly linked with the surrounding NaO_6 octahedra, wherein the connection geometry of the NaO_6 octahedra in tincalconite has a three-dimensional framework with large cavities filled by the $\text{B}_4\text{O}_5(\text{OH})_4$ clusters. Notably, the B-O

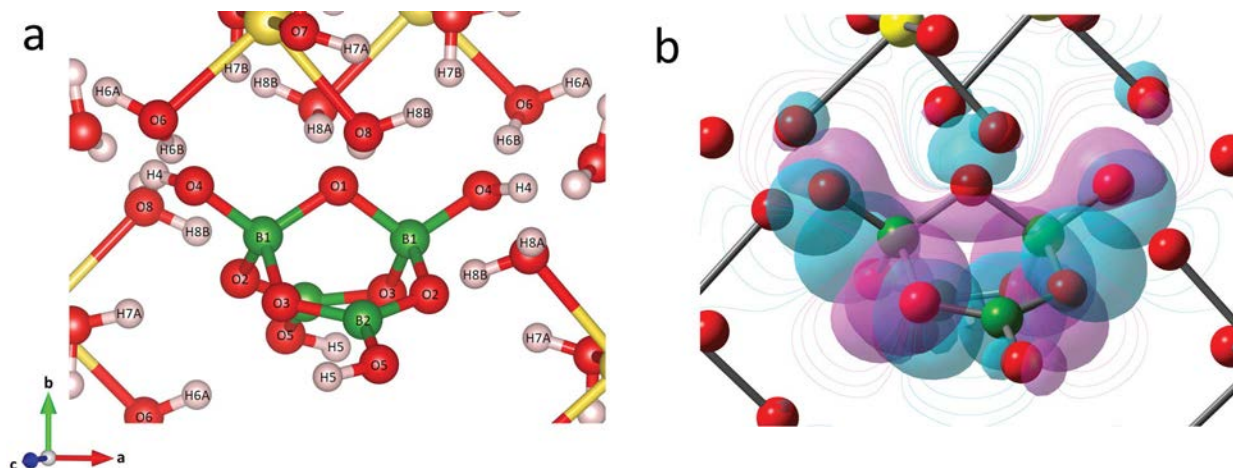


FIGURE 6. (a) Local environment around the isolated $\text{B}_4\text{O}_5(\text{OH})_4$ cluster and (b) the molecular orbitals. Sodium, boron, oxygen, and hydrogen atoms are shown as yellow, green, red, and pink spheres, respectively. The purple and light blue orbitals represent positive and negative wave functions, respectively. In **b**, the H atoms are not shown for clarity. The orbitals are drawn at an isosurface value of 0.02 au. Contours of the electron density isosurface are plotted on the a - c plane. (Color online.)

bond lengths and angles in the $\text{B}_4\text{O}_5(\text{OH})_4$ cluster are essentially invariant before and after the phase transition of borax. The nature of a rigid FBB might be effective for the rapid and reversible phase transition between borax and tinalconite. After the dehydration of tinalconite, the $\text{B}_4\text{O}_5(\text{OH})_4$ cluster itself should remain stable until the crystallization of the anhydrous borax phases: α - $\text{Na}_2\text{B}_4\text{O}_7$ and γ - $\text{Na}_2\text{B}_4\text{O}_7$ (Nishiyasu and Kyono 2023).

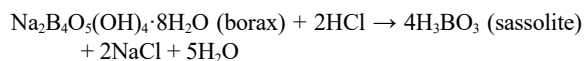
Molecular orbital surface of the isolated $\text{B}_4\text{O}_5(\text{OH})_4$ cluster

Burns (1995) evaluated cluster geometries consisting of four borate polyhedra by the Hartree-Fock method using the 3-21G* basis set. His results indicated that the most stable cluster comprises double three-membered rings consisting of one $\text{B}\phi_3$ triangle and two $\text{B}\phi_4$ tetrahedra expressed as $\langle\Delta 2\Box\rangle=\langle\Delta 2\Box\rangle$. The FBB of the isolated $\text{B}_4\text{O}_5(\text{OH})_4$ cluster and its MO are shown in Figure 6. The MO is largely localized in the cluster as positive (purple) and negative (light blue) electron clouds. An observed characteristic feature is that a positive electron cloud is shared by the two borate tetrahedra, leading to the formation of a large electron cloud distribution over O4-B1-O1-B1-O4. The shared electron cloud possesses a covalent bonding characteristic. A negative electron cloud is also shared between two O3 atoms, and thus, the electron cloud yields another covalent bond in the cluster. It is important to emphasize that the intramolecular interactions with substantial covalent character make the cluster quite rigid. In contrast, after the phase transition, the arrangement of the NaO_6 octahedra readily changes from the zigzag chain to a three-dimensional framework with large cavities. Notably, the rigidity of the isolated $\text{B}_4\text{O}_5(\text{OH})_4$ cluster and the flexibility of the NaO_6 octahedral connection geometry can lead to a large structural modification between borax and tinalconite without any significant energy requirements.

IMPLICATIONS

Borate minerals display extensive structural complexity resulting from the great diversity of FBBs. The structural chemistry of borate is quite similar to that of silicate. In particular, the $\text{B}\phi_3$,

$\text{B}\phi_4$, and $\text{Si}\phi_4$ groups (ϕ : O^{2-} , OH) have a marked tendency to polymerize in the solid, which gives rise to the structural complexity of both groups. Burns et al. (1995) examined topologically possible clusters of borates and indicated that there are nine types of clusters consisting solely of $\text{B}\phi_3$ triangles, 39 types of clusters consisting solely of $\text{B}\phi_4$ tetrahedra, and 108 clusters consisting of both $\text{B}\phi_3$ triangles and $\text{B}\phi_4$ tetrahedra. Most of these clusters are not observed in borate minerals, while several types are very common. Furthermore, Burns et al. (1995) described that the connection geometry that includes a three-membered ring consisting of one $\text{B}\phi_3$ triangle and two $\text{B}\phi_4$ tetrahedra expressed as $\langle\Delta 2\Box\rangle$ seems to be favored relative to other possible combinations. The $\langle\Delta 2\Box\rangle=\langle\Delta 2\Box\rangle$ cluster is a common FBB in borate minerals, e.g., in borax $\text{Na}_2\text{B}_4\text{O}_5(\text{OH})_4 \cdot 8\text{H}_2\text{O}$ (Levy and Lisensky 1978), tinalconite $\text{Na}_2\text{B}_4\text{O}_5(\text{OH})_4 \cdot 3\text{H}_2\text{O}$ (Luck and Wang 2002), hungchaoite $\text{MgB}_4\text{O}_5(\text{OH})_4 \cdot 7\text{H}_2\text{O}$ (Wan and Ghose 1977), fedorovskite $\text{Ca}_2\text{Mg}_2\text{B}_4\text{O}_7(\text{OH})_6$ (Kobayashi et al. 2020), and roweite $\text{Ca}_2\text{Mn}_2^+\text{B}_4\text{O}_7(\text{OH})_6$ (Moore and Araki 1974). Our study revealed that a large electron cloud shared by the two borate tetrahedra leads to an extremely rigid $\langle\Delta 2\Box\rangle=\langle\Delta 2\Box\rangle$ cluster. Borax is quite soluble in water (4.81 g/100 mL 20 °C; Garrett 1998) but is readily recrystallized from saturated water. It is therefore highly possible that the $\langle\Delta 2\Box\rangle=\langle\Delta 2\Box\rangle$ cluster exists in water as it is. In addition, consideration of the stability at high temperatures indicates that the $\langle\Delta 2\Box\rangle=\langle\Delta 2\Box\rangle$ cluster will be stable under hydrothermal conditions. On the other hand, borax is unstable in strong acid solutions and its dissociation leads to the formation of sassolite as follows:



The FBBs in sassolite comprise isolated $\text{B}\phi_3$ triangles expressed as 1Δ (Gajhede et al. 1986). Thus, once the $\langle\Delta 2\Box\rangle=\langle\Delta 2\Box\rangle$ cluster is formed, it is very stable as long as it is not exposed to strong acidic environments. In conclusion, the existence of borate minerals containing the $\langle\Delta 2\Box\rangle=\langle\Delta 2\Box\rangle$ cluster should evidence the

existence of moderately acidic or alkaline water where the borate minerals were grown via the incorporation of $(\Delta 2\Box) = (\Delta 2\Box)$ clusters. These types of clusters consisting of $\text{B}\phi_3$ triangles and $\text{B}\phi_4$ tetrahedra in borate minerals can potentially be used as a palaeoenvironmental indicator.

FUNDING

The synchrotron radiation experiment performed at BL8B at KEK-PF was approved by the Photon Factory Program Advisory Committee (Proposal Nos. 2019G115 and 2021G521). This work was supported by JSPS KAKENHI grant number JP20K04124). This work was supported by KAKENHI (grant number JP20K04124) granted to Atsushi Kyono.

REFERENCES CITED

- Bindeman, I.N., Davis, A.M., and Drake, M.J. (1998) Ion microprobe study of plagioclase-basalt partition experiments at natural concentration levels of trace elements. *Geochimica et Cosmochimica Acta*, 62, 1175–1193, [https://doi.org/10.1016/S0016-7037\(98\)00047-7](https://doi.org/10.1016/S0016-7037(98)00047-7).
- Bruker. (2017) SAINT Version 8.38A. Bruker Analytical X-ray Instruments Inc.
- (2018) APEX3, Version 2018.1. Bruker Analytical X-ray Instruments Inc.
- Burns, P.C. (1995) Borate clusters and fundamental building blocks containing four polyhedra: Why few clusters are utilized as fundamental building blocks of structures. *Canadian Mineralogist*, 33, 1167–1176.
- Burns, P.C., Grice, J.D., and Hawthorne, F.C. (1995) Borate minerals; I. Polyhedral clusters and fundamental building blocks. *Canadian Mineralogist*, 33, 1131–1151.
- Christ, C.L. and Garrels, R.M. (1959) Relations among sodium borate hydrates at the Kramer deposit, Boron, California. *American Journal of Science*, 257, 516–528, <https://doi.org/10.2475/ajs.257.7.516>.
- Dennington, R., Keith, T.A., and Millam, J.M. (2016) GaussView, Version 6.1. Semichem Inc.
- Dumanli, F.T.S., Kipcak, A.S., and Derun, E.M. (2022) Microwave dehydration of borax: Characterization, dehydration kinetics, and modelling. *Glass Physics and Chemistry*, 48, 210–218, <https://doi.org/10.1134/S1087659622030087>.
- Ekmekyapar, A., Baysar, A., and Kunkul, A. (1997) Dehydration kinetics of tincal and borax by thermal analysis. *Industrial & Engineering Chemistry Research*, 36, 3487–3490, <https://doi.org/10.1021/ie970018r>.
- Frisch, M.J., Trucks, G.W., Schlegel, H.B., Scuseria, G.E., Robb, M.A., Cheeseman, J.R., Scalmani, G., Barone, V., Petersson, G.A., Nakatsuji, H., and others. (2016) *Gaussian 16*, Revision C.01. Gaussian, Inc.
- Gajhede, M., Larsen, S., and Rettrup, S. (1986) Electron density of orthoboric acid determined by X-ray diffraction at 105 K and *ab initio* calculations. *Acta Crystallographica Section B, Structural Science*, 42, 545–552, <https://doi.org/10.1107/S0108768186097720>.
- Garrett, D.E. (1998) Borates: Handbook of Deposits, Processing, Properties, and Use, 483 p. Academic Press.
- Giacovazzo, C., Menchetti, S., and Scordari, F. (1973) The crystal structure of tincalconite. *American Mineralogist*, 58, 523–530.
- Helvacı, C. and Palmer, M.R. (2017) Origin and distribution of evaporite borates: The primary economic sources of boron. *Elements*, 13, 249–254, <https://doi.org/10.2138/gselements.13.4.249>.
- Kobayashi, S., Higashino, F., Tanabe, M., Kishi, S., Ichihashi, Y., and Kusachi, I. (2020) Fedorovskite from the Fuka mine, Okayama Prefecture, Japan. *Journal of Mineralogical and Petrological Sciences*, 115, 479–484, <https://doi.org/10.2465/jmps.200512>.
- Krogh-Moe, J. (1962) The crystal structure of lithium diborate, $\text{Li}_2\text{O} \cdot 2\text{B}_2\text{O}_3$. *Acta Crystallographica*, 15, 190–193, <https://doi.org/10.1107/S0365110X6200050X>.
- Levy, H.A. and Lisensky, G.C. (1978) Crystal structures of sodium sulfate decahydrate (Glauber's salt) and sodium tetraborate decahydrate (borax). Redetermination by neutron diffraction. *Acta Crystallographica B: Structural Crystallography and Crystal Chemistry*, 34, 3502–3510, <https://doi.org/10.1107/S0567740878011504>.
- Luck, R.L. and Wang, G. (2002) On the nature of tincalconite. *American Mineralogist*, 87, 350–354, <https://doi.org/10.2138/am-2002-2-319>.
- Moore, P.B. and Araki, T. (1974) Roweite, $\text{Ca}_2\text{Mn}_2^{2+}(\text{OH})_4[\text{B}_4\text{O}_7(\text{OH})_2]$: Its atomic arrangement. *American Mineralogist*, 59, 60–65.
- Nishiyasu, W. and Kyono, A. (2023) Crystal structures of anhydrous borax $\alpha\text{-Na}_2\text{B}_4\text{O}_7$ and $\beta\text{-Na}_2\text{B}_4\text{O}_7$ and *ab initio* quantum chemical calculations of structural stability on their fundamental building blocks. *Journal of Mineralogical and Petrological Sciences*, 118, 010, <https://doi.org/10.2465/jmps.230112>.
- Raoux, S. and Wuttig, M., Eds. (2009) *Phase Change Materials: Science and Applications*, 430 p. Springer.
- Rossini, F.D., Wagman, D.D., Evans, W.H., Levine, S., and Jaffe, I. (1952) Selected values of chemical thermodynamic properties. Circular of the National Bureau of Standards 500. U.S. Government Printing Office.
- Rudnick, R.L. and Gao, S. (2014) Composition of the continental crust. In R.L. Rudnick, Ed., *The Crust. Treatise on Geochemistry*, 4, 1–51. Elsevier.
- Senkova, N., Bubnova, R., Shepelev, J., Filatov, S., and Yakovleva, O. (2007) $\text{Li}_2\text{B}_2\text{O}_7$ crystal structure in anharmonic approximation at 20, 200, 400 and 500 °C. *Journal of Alloys and Compounds*, 428, 290–296, <https://doi.org/10.1016/j.jallcom.2006.03.049>.
- Senyshyn, A., Schwarz, B., Lorenz, T., Adamiv, V.T., Burak, Y.V., Banys, J., Grigalaitis, R., Vasylechko, L., Ehrenberg, H., and Fuess, H. (2010) Low-temperature crystal structure, specific heat, and dielectric properties of lithium tetraborate $\text{Li}_2\text{B}_4\text{O}_7$. *Journal of Applied Physics*, 108, 093524, <https://doi.org/10.1063/1.3504244>.
- Sharma, A., Tyagi, V.V., Chen, C.R., and Buddhi, D. (2009) Review on thermal energy storage with phase change materials and applications. *Renewable & Sustainable Energy Reviews*, 13, 318–345, <https://doi.org/10.1016/j.rser.2007.10.005>.
- Shearer, C.K. and Simon, S.B. (2017) Boron behavior during the evolution of the early solar system: The first 180 million years. *Elements*, 13, 231–236, <https://doi.org/10.2138/gselements.13.4.231>.
- Sheldrick, G.M. (2008) A short history of SHELX. *Acta Crystallographica A: Foundations of Crystallography*, 64, 112–122, <https://doi.org/10.1107/S01087673070043930>.
- (2012) SADABS Version 2012/1. Bruker Analytical X-ray Instruments Inc.
- Simmons, W., Falster, A., Webber, K., Roda-Robles, E., Boudreaux, A.P., Grassi, L.R., and Freeman, G. (2016) Bulk composition of Mt. Mica pegmatite, Maine, USA: Implications for the origin of an LCT type pegmatite by anatexis. *Canadian Mineralogist*, 54, 1053–1070, <https://doi.org/10.3749/canmin.1600017>.
- Stilling, A., Černý, P., and Vanstone, P.J. (2006) The Tanco pegmatite at Bernic Lake, Manitoba. XVI. Zonal and bulk compositions and their petrogenetic significance. *Canadian Mineralogist*, 44, 599–623, <https://doi.org/10.2113/gscanmin.44.3.599>.
- Waclawska, I. (1995) Thermal decomposition of borax. *Journal of Thermal Analysis and Calorimetry*, 43, 261–269, <https://doi.org/10.1007/BF02635993>.
- Wan, C. and Ghose, S. (1977) Hungchaoite, $\text{Mg}(\text{H}_2\text{O})_2\text{B}_4\text{O}_7(\text{OH})_4 \cdot 2\text{H}_2\text{O}$: a hydrogen-bonded molecular complex. *American Mineralogist*, 62, 1135–1143.
- Wunder, B., Meixner, A., Romer, R.L., Wirth, R., and Heinrich, W. (2005) The geochemical cycle of boron: Constraints from boron isotope partitioning experiments between mica and fluid. *Lithos*, 84, 206–216, <https://doi.org/10.1016/j.lithos.2005.02.003>.
- Zhou, D., Zhao, C.Y., and Tian, Y. (2012) Review on thermal energy storage with phase change materials (PCMs) in building applications. *Applied Energy*, 92, 593–605, <https://doi.org/10.1016/j.apenergy.2011.08.025>.

MANUSCRIPT RECEIVED FEBRUARY 10, 2023

MANUSCRIPT ACCEPTED MAY 17, 2023

ACCEPTED MANUSCRIPT ONLINE MAY 25, 2023

MANUSCRIPT HANDLED BY G. DIEGO GAITA

Endnote:

¹Deposit item AM-24-38970. Online Materials are free to all readers. Go online, via the table of contents or article view, and find the tab or link for supplemental materials. The CIF has been peer-reviewed by our Technical Editors.